Online time-resolved reconstruction method for acoustic tomography system

Online time-resolved reconstruction method for acoustic tomography system

Yong Bao, Member, IEEE, and Jiabin Jia, Senior Member, IEEE

***Abstract*— Acoustic tomography can deliver accurate quantitative reconstruction of the covered temperature distribution with low equipment cost. For the application of real-time temperature field monitoring, both the temporal resolution and reconstruction speed are of great significance. In this paper, we developed a novel online time-resolved reconstruction (OTRR) methods, which can improve temporal resolution to capture dynamic changes and accelerate the tomographic reconstruction process for online real-time monitoring. Firstly, by exploiting the redundancy of the temporal information, a temporal regularisation is designed based on adaptive auto aggressive (AR) model to reduce the required amount of TOF data per frame. A sliding overlapping window is applied to further improve the reconstruction accuracy. Secondly, recursive reconstruction process performs a sliding iteration over each data segment. For the reconstruction of each frame, the online computation is non-iterative. Numerical simulation and lab-scale experiment are performed to validate the proposed OTRR method. The reconstruction images are compared with the online time-resolved reconstruction methods based on Kalman filter. Results show that our method can improve the temporal resolution the computational time and produce acceptable results.**

Keyword: time-resolved tomography; online reconstruction; acoustic tomography.

I. INTRODUCTION

Acoustic tomography utilizes the TOF measurements along multiple sound propagation ray paths to reconstruct the sound speed distribution[1]. Based on the reconstructed sound speed distribution, the internal structure and properties of the medium, for instance, the air temperature distribution within the sensing area can be estimated. Owing to its non-invasive nature, fast imaging speed, low equipment cost and scalability for variety of measurement range, acoustic tomography has attracted considerable interest in various applications[2]. Well-investigated applications using acoustic tomography include the near surface atmosphere temperature and wind velocity monitoring[3-5], the furnace boiler temperature field measurement[6, 7], medical ultrasound[8-11], and ocean current monitoring imaging[12].

Our previous study focus on the imaging of static temperature field[1]. However, the acoustic tomography system may lack a sufficient temporal resolution to reconstruct the dynamic features of some fast-changing temperature fields. The temperature changes during the measuring time of each frame, for example, the motion of heat source, will blur the tomographic image and affect the temperature reconstruction accuracy. Research has tended to focus on accelerating the data acquisition process to improve the temporal resolution, with the use of broadband acoustic transducers and parallel data collection. Unfortunately, due to hardware limitations and the high implemental cost of the air ultrasonic transducers, it is generally difficult to apply a fully parallel data acquisition of measuring the TOFs along all transmission ray paths simultaneously. Besides, the minimum data acquisition time for each ray path is limited by the speed of sound and the size of sensing area. For our lab-scale experimental setup, the 1 m^2 sensing area requires a minimum of 20 ms measuring time for the longest ray path to propagate.

Besides reducing the data acquisition time, an alternative way is to use a smaller number of TOFs per frame and reconstruct an under-sampled tomographic image of the temperature field. Consequently, the measuring time per frame is largely reduced and the temporal resolution can be greatly improved.

Under-sampled reconstruction with fewer TOFs can improve the temporal resolution, but it also brings aliasing artefacts in image space. Compared to the conventional fully sampled tomographic reconstruction, this under-sampled reconstructed image suffers from the lack of spatial resolution to resolve the temperature field distribution [13]. Fortunately, the redundancy of information in the temporal domain can be employed to solve this problem. The temporal redundancy provides additional information for the tomographic reconstruction of each frame. Serval time-resolved image reconstruction methods were developed [13-18]. These time-resolved imaging algorithms were able to reconstruct the high-quality tomographic image from under-sampled data sets and resolved the dynamic changes which could not be recognised by the conventional fully-sampled tomographic reconstruction. Generally, these time-resolved reconstruction methods can be categorised into three main branches.

In the first branch, the temporal redundancy across consecutive frames is used to build different regularisation term in the algebraic-based reconstruction. These regularisations are designed for a specific application, such as temporal smoothness regularisation for general cases, spatial-temporal total variation for the temporal piecewise constant data, temporal non-local means regularisation for the structural similarity between frames, and nuclear norm regularisation for the low-rank structure of a time series data [16, 17, 19]. These methods are able to reconstruct images with good quantitative accuracy using very few data. However, most of the methods require iterative reconstruction, which is more suitable for offline reconstruction rather than online reconstruction for real-time monitoring.

Another approach of the time-resolved reconstruction method is based on the Karhunen Louve transform (KLT), where the temporal redundancy information is extracted from the data [13, 20-22]. It utilises the sparse representation of

image series under KLT domain with the temporal basis functions. The temporal basis functions can be obtained from under-sampled reconstructed images. However, these methods rely on the implicit assumption that the principal basis functions estimated from the low-resolution data closely approximate the original KLT basis functions. Clearly, this approximation requires a sufficient number of measurements in the training data. Besides, it is also an offline iterative reconstruction method and not suitable for real-time monitoring.

Thirdly, there is also a statistical approach of time-resolved reconstruction based on the Kalman filter or the unscented Kalman filter [23, 24]. The tomographic reconstruction problem is formulated as a state estimation problem and the temporal redundancy can be interpreted into the state transition model of the Kalman filter. It has the advantages of fast reconstruction and online reconstruction potential. However, there is still a problem with this approach. The Kalman filter reconstruction requires that the state transition error is Gaussian, but it is not always the case. It is necessary to find a whitening transform for the state transition model, which will significantly increase the complexity of the algorithm [19].

In this paper, we developed an online time-resolved reconstruction method, which is able to reconstruct high quality time-resolved images using fewer TOFs per frame. Our main novelties can be summarized as follow. Firstly, by exploiting the redundancy of information in the temporal domain, a temporal regularisation is designed based on adaptive auto aggressive (AR) model to reduce the required amount of TOF data per frame. A sliding overlapping window is applied to further improve the reconstruction accuracy. Secondly, a non-iteration scheme is used for the time-resolved reconstruction. Instead of conducting iterative calculation upon each data set until convergence, the recursive reconstruction process performs a sliding iteration over each data segment. For the reconstruction of each frame, the online computation is non-iterative.

II. METHODS

A. Fundamental of acoustic tomography

1) Forward problem

The forward problem of acoustic tomography establishes the relationship between the TOF measurements and the speed of sound which is dependent on temperature. Given the sound propagation ray paths, the temperature field distribution can be reconstructed from the TOF measurements. Throughout literature, the straight ray model has been widely used to approximate the true propagation ray path with a straight line connecting the transmitter and receiver. The modelling error for using the straight ray model was quantitatively investigated [25], which showed that the straight ray model can be applied for small-scale measurement setups.

The TOFs and images for all the frames of the tomographic images can be stacked as columns and denoted as $\boldsymbol{X} = [\boldsymbol{x}_1, \boldsymbol{x}_2, \dots, \boldsymbol{x}_T]$ and $\boldsymbol{Y} = [\boldsymbol{y}_1, \boldsymbol{y}_2, \dots, \boldsymbol{y}_T]$, where T is the number of frames. Then the forward problem can be written as $\boldsymbol{Y} = \boldsymbol{A}\boldsymbol{X}$, where the block diagonal matrix $\boldsymbol{A}$ is given as $\boldsymbol{A} = diag\{\boldsymbol{A}_1, \boldsymbol{A}_2, \dots, \boldsymbol{A}_T\}$ .The forward problem for frame t is defined as:

$$\boldsymbol{y}_t = \boldsymbol{A}_t \boldsymbol{x}_t, \quad t = 1, 2, \dots, T \tag{1}$$

where $\boldsymbol{x}_t \in \mathbb{R}^{N\times 1}$ denotes the tomographic image vector which describes the travel speed reduction distribution and N is the pixel number. Its element $x_{t,j} = 1/c_{L,j}(Temp)$ is the speed reduction in the j-th pixel. $\boldsymbol{y}_t \in \mathbb{R}^{M\times 1}$ as the TOFs measurement vector and M is the measurement number for each frame. $\boldsymbol{A}_t \in \mathbb{R}^{M\times N}$ represents the ray length matrix for frame t and its element $a_{i,j}$ is the segment length for each ray path across one pixel. $c_{L,j}(Temp_j) = \sqrt{R\gamma Temp_j}$ is Laplace's speed of sound in the j-th pixel, where $Temp_j$ denotes the temperature at j-th pixel, $R = 287\ J\ kg^{-1}\ K^{-1}$ is the gas constant and $\gamma = 1.4$ is the specific heat ratio assuming a constant gas composition[1].

The tomographic reconstruction firstly obtains the speed of sound which is a function of the temperature distribution. Subsequently, the temperature distribution can be estimated from the TOF by solving a tomographic inverse problem.

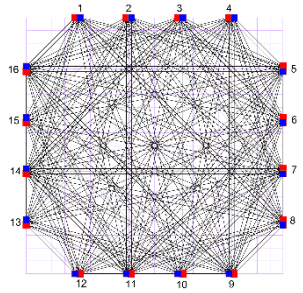

Figure 1: Tomographic experiment setup with 16 transmitters (red points) and 16 receivers (blue points).

2) TOF data acquisition

The measurement setup of the acoustic travel-time tomography system is illustrated in Figure 1. 16 transmitters and 16 receivers are placed with uniform spacing around the boundary of the sensing area. They form 192 transducer pairs which are used to measure the TOFs. Currently, a semi-parallel data collection scheme is used. In the experiments, all transmitters are activated sequentially every 10 ms, and during each 10 ms repetition period, all the received waveforms at different receivers are measured simultaneously. The total measuring time for each frame is 20ms *16=320 ms. Therefore, the acoustic tomography system is not able to resolve dynamic changes within the 320 ms measuring time.

There are two ways to improve the temporal resolution of the acoustic tomography system: (1) reducing the TOFs measuring time; and (2) reducing the number of TOFs per frame for reconstruction. In practical, it is very difficult to further reducing the TOFs measuring time and the reason is given as follow. Firstly, due to the transducer hardware limitation, it is very difficult to find an appropriate broadband ultrasound transmitter for fully parallel data collection to reduce the measuring time. Secondly, accurate TOF estimation requires that the repetition period should be around 20 ms. If the repetition period less than 20 ms, there will be considerable

interference from the previous signal sent from another transmitter. Therefore, reducing the number of TOFs per frame is the only way to improve the temporal resolution. If a minimum number of 36 TOFs corresponding to three transmitters are used for each frame, then the temporal resolution can be greatly improved from 320 ms to 60 ms.

B. OTRR method

The temporal resolution of the acoustic tomography system can be greatly improved if fewer TOFs are used for the reconstruction per frame. However, the improvement of temporal resolution is at the cost of spatial resolution of the reconstructed image. Reconstruction with fewer TOFs will introduce aliasing artefacts in image space. To solve this problem, temporal regularization is applied in the proposed time-resolved tomographic reconstruction method and details is presented as follow.

1) Inverse problem and objective function

The regularized inverse problem is defined as below.

$$\boldsymbol{X} = \min_{\boldsymbol{X}} \left\| \boldsymbol{Y} - \boldsymbol{AX} \right\|_{\mathrm{F}}^2 + \alpha_1 \sum_{t=1}^{T} \left\| \boldsymbol{F}\boldsymbol{x}_t \right\|_2^2 + \alpha_2 \boldsymbol{R(X)} \tag{2}$$

where $\|\boldsymbol{F}\boldsymbol{x}_t\|_2$ is used to enforce spatial smoothness for each frame, and $\boldsymbol{F}$ is a linear differential operator [26]. $\boldsymbol{R}(\boldsymbol{X})$ is used to enforce temporal regularity for the time series. $\boldsymbol{\alpha_1}$ and $\boldsymbol{\alpha_2}$ are two predefined regularization parameters.

2) Temporal regularization

Various temporal regularization methods have been developed to improve the spatial resolution for the time-resolved tomographic reconstruction. For example, in the case of Electrical Resistance Tomography (ERT) where the consecutive frames can be well approximated by a piecewise constant function, the spatial-temporal Total Variation regularization is selected for the tomographic reconstruction[16]. With dynamic MRI used for medical imaging, where the MRI sequence can be approximated by a low rank matrix, nuclear norm can be used for the tomographic reconstruction [19]. Another case is the 4DCT, where the structure similarity across consecutive frames is used to build the non-local mean regularization for reconstruction. However, these regularizations are not suitable to be used here for two reasons: (1) the dynamic temperature field is generally smooth on the time domain, and they do not have the aforementioned features; and (2) spatial-temporal TV, nonlocal mean regularization and low rank regularization methods require iterative computation, which may not be suitable for fast online reconstruction.

Temporal smoothing regularization is applied in the proposed OTRR method based on the assumption of similarity of the reconstructed frames [14]. Apart from this temporal smoothing regularization, no other prior knowledge is used for any specific target temperature field. Generally, the temporal regularization is designed based on the difference among successive frames.

$$\boldsymbol{R(X)} = \sum_{t=2}^{T} \left\| \boldsymbol{x_t} - \boldsymbol{x_{t-1}} \right\|_2^2 \tag{3}$$

In the cases when the dynamic characteristics happen within the region of interest and the motion is hard to predict, using more frames instead of only adjacent time frames will significantly improve the reconstruction quality [14]. Here an adaptive AR model is applied. For a group of time series, we define the AR prediction for frame t $\boldsymbol{x}_t^*$as

$$\boldsymbol{x}_t^* = \sum_{k=1}^{T} w_t(k) \boldsymbol{x_k} = \boldsymbol{X}\boldsymbol{w_t} \tag{4}$$

where $\boldsymbol{w}_t \in \mathbb{R}^{T\times 1}$ is a normalized AR weights defined as

$$w_t(k) = \frac{e^{-(k-t)^2/\rho}}{\sum_{k=1}^{T} e^{-(k-t)^2/\rho}},\ k = 1,2,...,T \tag{5}$$

where ρ is the smoothing parameter. Therefore we can define a penalty term based on this AR model as

$$\boldsymbol{R(X)} = \sum_{t=1}^{T} \boldsymbol{R}(\boldsymbol{x}_t) = \sum_{t=1}^{T} \left\| \boldsymbol{X}\boldsymbol{w}_t - \boldsymbol{x}_t \right\|_2^2 \tag{6}$$

3) Iterative reconstruction

To solve the inverse problem, we firstly split the inverse problem into two sub problem based on the forward–backward splitting method (FBS)[27].

$$\boldsymbol{X}^{i+1/2} = \min_{\boldsymbol{X}} \left\| \boldsymbol{Y} - \boldsymbol{AX} \right\|_2^2 + \alpha_1 \sum_{t=1}^{T} \left\| \boldsymbol{F}\boldsymbol{x}_t \right\|_2^2 \tag{7}$$

$$\boldsymbol{X}^{i+1} = \min_{\boldsymbol{X}} \left\| \boldsymbol{X} - \boldsymbol{X}^{i+1/2} \right\|_2^2 + \alpha_2 \boldsymbol{R(X)} \tag{8}$$

Sub-problem 1 involved the data fidelity and spatial regularization term, and do not include the temporal regularization term. Therefore, each frame can be reconstructed independently.

$$x_t^{i+1/2} = \min_{x} \left\| \boldsymbol{y_t} - \boldsymbol{A_t}\boldsymbol{x_t} \right\|_2^2 + \alpha_1 \left\| \boldsymbol{F}\boldsymbol{x_t} \right\|_2^2 \tag{9}$$

It can be solved by our modified SIRT using online reconstruction and offline iteration method[26].

$$\begin{aligned} \boldsymbol{x}_t^{i+1/2,m} = \boldsymbol{x}_t^{i+1/2,m-1} + \boldsymbol{P}\boldsymbol{A}_t^T \boldsymbol{W}(\boldsymbol{y} - \boldsymbol{A}_t \boldsymbol{x}_t^{i+1/2,m-1}) \\ -\lambda \boldsymbol{P}\boldsymbol{F}^{\boldsymbol{T}} \boldsymbol{F}\boldsymbol{x}_t^{i+1/2,m-1} \end{aligned} \tag{10}$$

$\boldsymbol{P}$ is the diagonal preconditioner: $\boldsymbol{P} = \mathrm{diag}(1/LP_1, 1/LP_2, \ldots, 1/LP_N)$, and $\mathbf{W}$ is the Normalised weight operator: $\mathbf{W} = \mathrm{diag}(1/LR_1, 1/LR_2, \ldots, 1/LR_M)$, where $LP_j = \sum_{i=1}^{M} a_{i,j}$, $LR_i = \sum_{j=1}^{N} a_{i,j}$. m denotes the inner iteration index for sub problem 1.

Then we stack the images as:

$$\boldsymbol{X}^{i+1/2} = \left[\boldsymbol{x}_1^{i+1/2}, \boldsymbol{x}_2^{i+1/2}, ..., \boldsymbol{x}_T^{i+1/2} \right] \tag{11}$$

Which can be used to solve the sub-problem 2.

For the sub-problem 2

$$\begin{aligned} \boldsymbol{X}^{i+1} &= \min_{X} \left\| \boldsymbol{X} - \boldsymbol{X}^{i+1/2} \right\|_F^2 + \sum_{t=1}^{T} \alpha_2 \left\| \boldsymbol{X}\boldsymbol{w}_t - x_t \right\|_2^2 \\ &= \min_{X} \sum_{t=1}^{T} \left\{ \left\| x_t^{i+1/2} - x_t \right\|_2^2 + \alpha_2 \left\| \boldsymbol{X}\boldsymbol{w}_t - \boldsymbol{x}_t \right\|_2^2 \right\} \end{aligned} \tag{12}$$

Once the image series $\boldsymbol{X}^{i+1/2}$ is obtained, we can solve it using one step gradient descent. This is because that we don't need to solve this sub-problem 2 very precisely for each i-th outer iteration.

$$\boldsymbol{x}_t^{i+1} = \boldsymbol{x}_t^{i+1/2} + \alpha_2 (\boldsymbol{X}\boldsymbol{w}_t - x_t^{i+1/2}) \tag{13}$$

Then

$$\boldsymbol{X}^{i+1} = \left[\boldsymbol{x}_1^{i+1}, \ldots, \boldsymbol{x}_T^{i+1} \right] \tag{14}$$

In summary, the reconstruction process is illustrated as below:

Input: $\boldsymbol{Y}$, $\boldsymbol{A}$, IterNo, $\boldsymbol{F}$, w, K, ϵ

Output: $\boldsymbol{X}$

Initialize: $\boldsymbol{X^0}$**=0**

For i=1: IterNo

For t=1: T

$$\boldsymbol{x_t^{i+1/2}} = \min_{\boldsymbol{x_t}} \|\boldsymbol{y}_t - \boldsymbol{A}_t \boldsymbol{x}_t\|_2^2 + \boldsymbol{\alpha_1} \|\boldsymbol{F}\boldsymbol{x}_t\|_2^2$$

End

$$\boldsymbol{X^{i+1/2}} = [\boldsymbol{x_1^{i+1/2}}, \boldsymbol{x_2^{i+1/2}}, \ldots, \boldsymbol{x_T^{i+1/2}}]$$

$$\boldsymbol{X^{i+1}} = \min_{\boldsymbol{X}} \left\| \boldsymbol{X} - \boldsymbol{X^{i+1/2}} \right\|_{\boldsymbol{F}}^2 + \sum_{\boldsymbol{t=1}}^{\boldsymbol{T}} \boldsymbol{\alpha_2} \{ \|\boldsymbol{X}\boldsymbol{w}_t - \boldsymbol{x}_t\|_2^2 \}$$

If $\left\| \boldsymbol{X^{i+1}} - \boldsymbol{X^i} \right\|_F^2 \leq \epsilon$ break

End

---

4) Segmentation for large group of data set

For the reconstruction of a large number of tomographic images, it is necessary to divide the whole data set into smaller segments and the reason is twofold. Firstly, the abovementioned time-resolved imaging method yield iterative procedures considering all the TOFs are measured and stored in advance, which will result in large computational cost. Secondly, it is not necessary to use all time frames to calculate the temporal regularization term, since the similarity between frames with large temporal distance is very weak. In this paper, each data segment consists of 16 frames' TOFs, and the frames of each segment can be reconstructed separately.

However, with the use of AR weights for temporal regularization, the reconstructed images at both ends of the segments will have larger reconstruction error compared to the images in the middle. For better reconstruction accuracy, we need to make sure that all the frames are reconstructed when they are in the middle of the segments. Therefore, the overlapped windowing data segmentation is used instead of non-overlapped windowing. An example of the overlapped windowing data segmentation is shown in Figure 2. A sliding window with the length of 16) and 50% overlapping is applied to the TOF data sets. The 8 frames within the middle of each segment (i.e. the frame 5-12 for the window 1 and frame 13-20 for the window 2) will be reconstructed since they are considered to have lower reconstruction error. Special cases are the first and last segments, where the reconstruction outputs will also contain the frame in the beginning and end. Due to the 50% overlapping sliding window, most of the frames are reconstructed when they behave as the middle frames of different segments. A comparison is shown in Figure 3. By using the overlapping window, the reconstruction errors of the frames at both ends of the non-overlapping window are reduced.

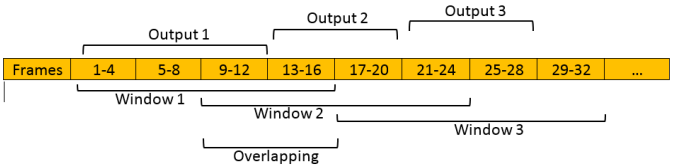

Figure 2: Data segmentation based on a sliding window.

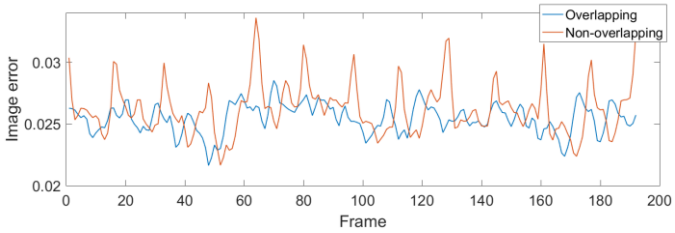

Figure 3: The comparison of the reconstruction error with non-overlapping segmentation (red) and 50%overlapping segmentation (blue)

The overlapping percentage is adjustable. A larger overlapping percentage helps to improve the temporal smoothness and continuity for the time series images, whereas, it also increases the computational cost. An appropriate overlapping percentage should be chosen for a specific application.

5) Recursive online reconstruction

Iterative computation is conducted to solve the two sub-problems on each data segment until convergence, which is not suitable for online monitoring system due to the large computational cost. To accelerate the reconstruction process, a recursive online reconstruction is applied. the general idea is to use the reconstruction results of the previous data segment as the initial guess to reconstruct the frames in the next segment. Higher overlapping percentages help to improve the temporal correlation between segments. As a result, the outer loop iteration number IterNo can be reduced. In this paper, the overlapping percentage can be set to the highest level. For the 16 order AR model here, the overlapping percentage is increased to 15/16=0.9375, which enables us to cancel the outer loop and set the IterNo to one. Since both sub-problems are solved non-iteratively, the reconstruction of each data segment

becomes non-iterative. A special case is the first segment since it is solved iteratively.

6) Connection with previous works

The dynamic tomographic reconstruction method using Kalman filter has been successfully applied in acoustic tomography, electrical tomography, dynamic MRI and etc [19, 23, 24, 28]. Different from algebraic-based algorithm, the Kalman filter reconstruction is a statistical-based method, which formulates the tomographic inverse problem as a state estimation. The reconstruction of the temperature distribution utilize both the information from TOFs measurements and the prior knowledge from the temporal evolution from the state transfer model [28]. Similar to the OTRR methods, this method also has the advantage of time-resolved imaging and non-iterative reconstruction. Generally, the state transfer and measurement equations are presented below.

$$\boldsymbol{x_t} = \boldsymbol{P}\boldsymbol{x_{t-1}} + \boldsymbol{w_t} \tag{15}$$

$$\boldsymbol{y_t} = \boldsymbol{A_t}\boldsymbol{x_t} + \boldsymbol{n} \tag{16}$$

where $\boldsymbol{P}$ is the state transition matrix based on a spatial-temporal AR model, which describe the relationship between consecutive frames [29]. For the estimation of temperature field is to minimize the following cost function:

$$x_t = \min_X \left\| \boldsymbol{y_t} - \boldsymbol{A_t}\boldsymbol{x_t} \right\|^2_{\Gamma_t^n} + \left\| \boldsymbol{x_t} - \boldsymbol{P}\boldsymbol{x_{t-1}} \right\|^2_{C_{t+1|t}} \tag{17}$$

where the measurement noise n is considered as a Gaussian white noise, so its covariance matrix is set as $\boldsymbol{\Gamma_t^n} = diag(\sigma_1)$, and σ_1 is a predefined parameter. The prediction error w_t is considered as a Gaussian white noise too, so its covariance matrix is set as $\boldsymbol{\Gamma_t^w} = diag(\sigma_2)$, and σ_2 is another predefined parameter. $\boldsymbol{C_{t+1|t}}$ is the time update covariance matrix, which is updated for each frame. The reconstruction for each frame is completed in two steps.

Step 1: Update in measurement

$$\boldsymbol{K_t} = \boldsymbol{C_{t|t-1}}\boldsymbol{A_t^T}(\boldsymbol{A_t}\boldsymbol{C_{t|t-1}}\boldsymbol{A_t^T} + \boldsymbol{\Gamma_t})^{-1} \tag{18}$$

$$\boldsymbol{C_{t|t}} = [\boldsymbol{I} - \boldsymbol{K_t}\boldsymbol{A_t}]\boldsymbol{C_{t|t-1}} \tag{19}$$

$$\boldsymbol{x_t} = \boldsymbol{x_{t|t-1}} + \boldsymbol{K_t}(\boldsymbol{y_t} - \boldsymbol{A_t}\boldsymbol{x_{t|t-1}}) \tag{20}$$

Step 2: Update in prediction

$$\boldsymbol{C_{t+1|t}} = \boldsymbol{P}\boldsymbol{C_{t|t}}\boldsymbol{P^T} + \boldsymbol{\Gamma_t^w} \tag{21}$$

$$\boldsymbol{x_{t+1|t}} = \boldsymbol{P}\boldsymbol{x_t} \tag{22}$$

For the initial guess of the reconstruction, we set $\boldsymbol{x_{1|0}} = \boldsymbol{0}$ and $\boldsymbol{C_{1|0}} = \boldsymbol{0}$.

Compared to the algebraic time-resolved reconstruction, it also uses a temporal smoothing regularization. The difference is that: (1) only adjacent frames are used to calculate the temporal regularization, and (2) the temporal regularization is weighted by the state transfer error covariance.

However, as is illustrated in [19], the Kalman filter assume the prediction error $\boldsymbol{w_t}$ is Gaussian, due to motions or changes in concentration levels. Normally, these motions or changes are not random Gaussian, and thus it will not meet the demands of Kalman filtering. Besides, the Kalman filter based reconstruction has a slow convergence, that the reconstruction error of a few frames in the beginning is large. In comparison, new method has the flexibility to modify the reconstruction process of the first segments to be iterative, which will significantly improve the reconstruction error at the beginning.

III. Numerical Results and Discussion

In this section, the performance of the proposed method is evaluated with a series of numerical simulations. The sensor array setup is illustrated in Figure 1, which consists of 16 transmitters and 16 receivers. They form 192 transducer pairs to measure the TOFs. The data collection is based on the semi-parallel scheme. 16 transmitters are activated sequentially every 20 ms. During each 20 ms repetition period, all the received waveforms at different receivers are measured simultaneously. In this simulation, the temperature field changes are assumed to take place during each 60 ms repetition period. Therefore 36 TOFs from 3 transmitters are used for the reconstruction of each frame. The proposed OTRR method are compared with the Kalman filter reconstruction.

Although optimal parameters can be used to improve the reconstruction quality, all the tomographic reconstruction results in this paper are obtained using the same parameters. These empirical reconstruction parameters are given in table 1. The 1x1 m sensing area is segmented into 400 pixels in the image reconstruction process and the dimension of each pixel is 5x5 cm, as shown in Figure 1.

Table 1: Reconstruction parameters used in simulation

Parameter	Method	Value
N	OTRR/Kalman	400
M	OTRR/Kalman	36
α_1	OTRR/Kalman	0.01
α_2	OTRR	0.1
T	OTRR	16
IterNo	OTRR	200
ϵ	OTRR	1e-10
σ_1	Kalman	1e-12
σ_2	Kalman	1e-13

Three representative dynamic phantoms of the temperature field are simulated to evaluate the reconstruction performance, including the temperature field of a point heat source with periodic rapid temperature change, diffusive expanding shape change and rotational position change. There are 200 frames in total to be reconstructed, and the repetition period of the dynamic changes is 32 frames (1920 ms). The first 16 frames of the three simulated phantoms are shown in Figure 4.

To quantitatively evaluate the overall reconstruction quality using the two methods, image relative error (IE) is adopted. Besides the relative image error for tomographic reconstruction, another three metrics are used to evaluate the accuracy of the reconstructed temperature field.

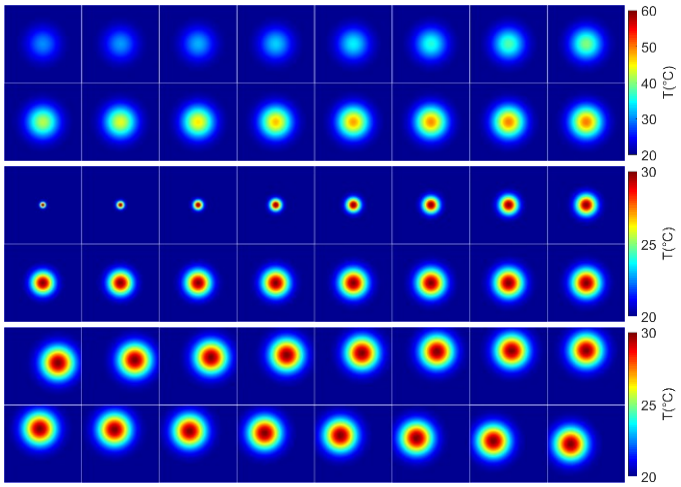

Figure 4: The three temperature phantoms of heating process (top) expanding (mid) and rotation (bottom)

Dislocation (DL) calculates the ratio of the distance between the heat source centre of the reconstructed and original temperature phantoms to the size of sensing area. DL evaluates the performance of the time-resolved reconstruction method on localizing the centre of the heat source. As small DL shows that the reconstruction method can resolve the motion of the heat source.

Peak value (PV) calculates the relative error of the reconstructed peak value of the temperature field to the original phantom. PV measures the quantitative accuracy of the temperature field reconstruction. As small PV shows that the reconstruction method can resolve the dynamic temperature changes.

Widening (WD) calculates the ratio of the reconstructed heated area to the original heated area. The average temperature is used as a threshold to extract the heated area from the temperature field images. WD measures the consistency of sizes of the estimated and target heated area. A high WD shows that the reconstruction method can resolve the dynamic heat source diffusion and expanding changes. Ideally, DL, PV and IE should be close to 0 but WD should be close to 1.

In this simulation, the measurement SNR is set to be 35dB, which is close to the measurement noise level of the lab scale acoustic tomography system. The mean value of the 4 quantitative metrics is presented in table 2. The convergence performance with respect to the image error is shown in Figure 5. The evolution of all the four metrics with respect to different measurement noise level are plotted in

Figure 6. The reconstructed images of the first 16 frames are given in Figure 7 and Figure 8.

Firstly, for reconstruction image error of all three phantoms, the proposed OTRR method has much better performance compared to the Kalman filter method. Notably, both methods have smaller reconstruction IE for phantom 2 than the other two phantoms. The reason is that the dynamic changes of the expanding phantom here are much smaller than the other two phantoms, and the temporal redundancy of this phantom 2 was utilized by the two time-resolved methods for a better reconstruction accuracy.

Secondly, for the DL metric, the proposed OTRR method outperforms the Kalman filter method as well. Especially for phantom3, where the dynamic change is mainly the rotation of the heat source. The OTRR method can accurately locate the dynamic heat centre with 4.57% location error, which is close to the reconstruction spatial resolution (5%). In comparison, the DL of Kalman filter method is 13.72%.

Thirdly, for the PV metrics, both methods lack the accuracy provide quantitative reconstruction of the dynamic temperature change of the heat centre. Although the OTRR has a slightly better performance for phantom 3, where the peak value of temperature doesn't change over time, its PV for other two phantoms are larger than 8%. The possible reason for PV inaccuracy is due to the over-smoothing on the temporal domain. Temporal regularization helps to reconstruct the temperature field images with fewer TOFs, but it also results in bias error in the reconstruction.

For the shape metric WD, the OTRR method also has better performance, especially for the reconstruction result of phantom 2, where the dynamic characteristics of the temperature is mainly about the expanding shape change. The WD of the OTRR method is 0.95, compared to the 0.74 of the Kalman filter method.

Table 2: The quantitative reconstruction metrics

		Phantom1	Phantom2	Phantom3
IE (%)	Kalman	7.3	4.34	7.67
	OTRR	4.25	2.99	4.21
DL (%)	Kalman	3.75	3.99	13.72
	OTRR	1.46	1.05	4.57
PV (%)	Kalman	12.79	11.65	15.93
	OTRR	8.82	8.86	5.92
WD (%)	Kalman	1.17	0.74	0.89
	OTRR	1.14	0.95	1.08

Figure 5 shows the convergence performance comparison of the two methods. Obviously, the OTRR method has a faster convergence compared to the Kalman filter method. This is because only the reconstruction of first segment is calculated iteratively when using the OTRR method. As a result, it is able to converge much faster than the Kalman filter method. The averaged computational time for the OTRR method is 6.51s. The computation time for Kalman is 0.57s for all 200 frames. Clearly, the Kalman filter method has much lower computational time compared to the OTRR method. The data acquisition system requires 60 ms to measure the received waveforms for 36 TOFs per frame. The 200 frames reconstruction time for OTRR is 6.51, and 32.55 ms per frame. This computational time per frame is less than the data collection time per frame. Therefore, the reconstruction can be conducted online without causing some computational delay.

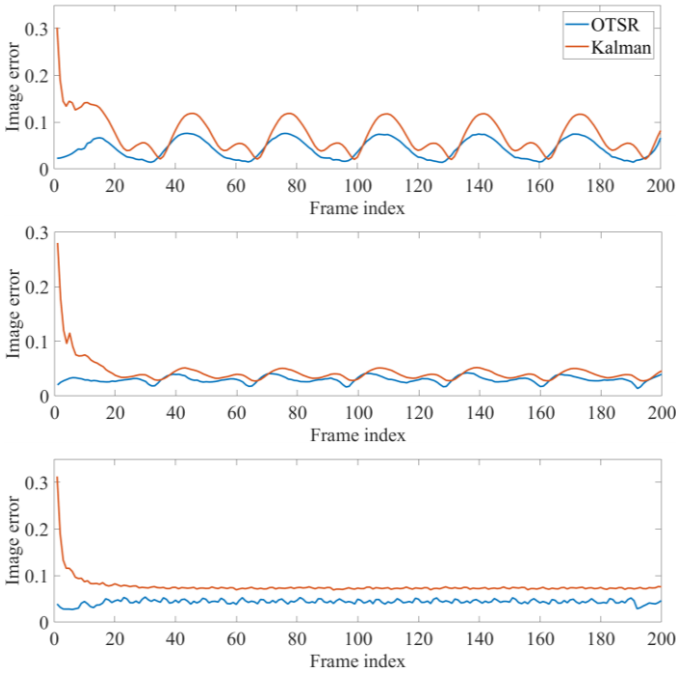

Figure 5: The reconstruction image errors of each frame for phantom 1 (top) phantom 2 (mid) and phantom 3 (bottom)

To evaluate the noise tolerance of the two methods, measurements at different noise level are used in the simulation. The averaged metrics under different SNR condition is plotted in

Figure 6. From the figure, it can be concluded the proposed OTRR method has a better noise tolerance than the Kalman filter method in terms of IE, DL and PV. For the shape metric WD, both methods have a good performance when the SNR is larger than 30 dB.

Figure 7 and Figure 8 show the reconstruction images of the first 16 frames. The proposed OTRR method has much better performance compared to the Kalman filter method. As can be seen from the figure, the Kalman filter method has large reconstruction error in the first few frames. The artefacts were reduced in the following frames, but the dynamic characteristic details are poorly preserved, especially for the phantoms 3. From the reconstructed images, it is very difficult to accurately locate the heat centre, estimate the peak value and track the shape changes of the temperature field. Compared to the Kalman filter method, the OTRR method can resolve the dynamic changes for all three phantoms. The temperature peak value increase, the heated area expanding, and the rotational location change of the heat centre are clearly described in the reconstructed images.

In conclusion, the simulation results show that the proposed OTRR method has better reconstruction accuracy, better noise tolerance, and faster convergence rate than the Kalman filter method.

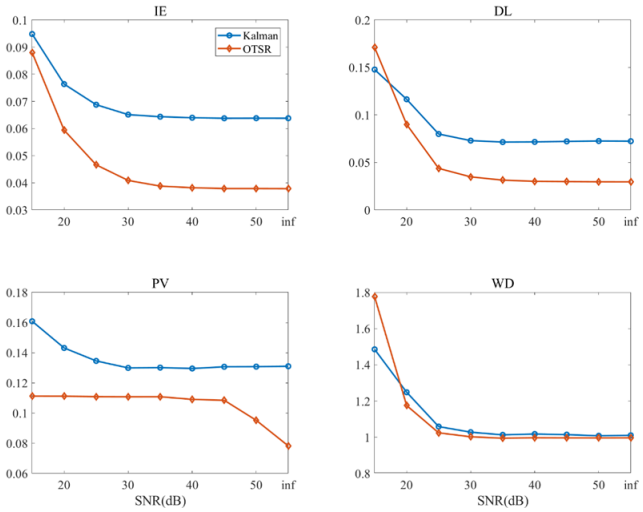

Figure 6: Quantitative metrics at different noise level

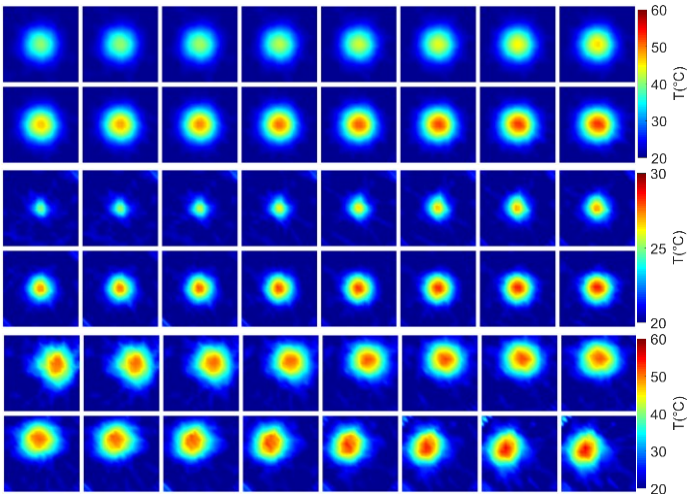

Figure 7: Reconstruction of the first 16 frames using OTRR

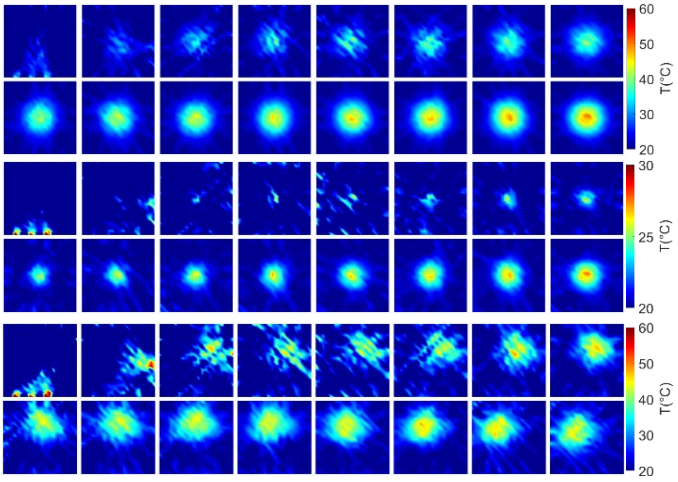

Figure 8: Reconstruction of the first 16 frames using Kalman

IV. Experimental Results and Discussion

An experimental study is presented to evaluate the performance of the proposed OTRR method. The ultrasound transmitters and receivers used in the experiments are 400ST120 and 400SR120, which operate at a resonant frequency of 40 kHz with 2 kHz bandwidth. The beam angle of the transducers is 120°, which allow each transmitter to simultaneously send ultrasound signals to 12 opposing receivers (also see Figure 1). As a result, the total number of TOF measurements for each frame is 192.

A hairdryer was placed 5 cm above the sensing plane to blow hot air downwards into the sensing area and create a hotspot. The acoustic tomography system was then used to reconstruct the temperature field. During the experiment, the hair dryer was placed in 8 different positions. For each position, after the hair dryer was switched on and the temperature had stabilised, 20 successive frames measurements were taken to test the repeatability of the temperature field reconstruction. For each frame's measurement, all the 192 TOFs are recorded for the fully sampled reconstruction. The fully sampled tomographic images using all the 192 TOFs will be reconstructed based on the conventional SIRT method[1]. For the hot spot temperature, a thermocouple was used to provide the pointwise temperature measurements. For the thermocouple, type K air temperature probe **(**model Testo 0602 1793**)** and thermometer (model RS PRO 1314 Digital Thermometer) were used. The measurement accuracy is ±0.05 % + 0.5 °C, and the measurement resolution is 0.1 °C. Both the fully sampled reconstruction image and the point wise thermocouple measurement are used to evaluate the performance the OTRR and the Kalman filter method. Like the numerical simulations, 36 TOFs from 3 transmitters were used for the reconstruction of the under-sampled frame. The measuring time for this 36 TOFs is 60 ms, which is the target temporal resolution. To evaluate the performance of OTRR, the hot spot is assumed to change every 60 ms.

Table 3: the temporal resolution comparison between fully sampled reconstruction and the OTRR method

	Fully sampled	OTRR
Temporal resolution	640 ms	60 ms

The comparison between the fully sampled tomographic reconstructions and the under-sampled reconstructions using both OTRR and Kalman filter method are presented in Figure 9. Using the fully sampled reconstruction results as the ground truth, then the quantitative reconstruction metrics, the IE, PV, DL and WD can be calculated, which are shown in Table 4.

The reconstruction results indicate that the under-sample images using OTRR method can resolve the position change of the hot spot, but the reconstructed image has large distortion compared to the fully sampled images. From table 3, the reconstruction accuracy using OTRR in terms of PV is very close to the fully-sampled reconstruction, which is 0.96%. However, the averaged WD is relatively large (3.54), which shows that the OTRR method does not have the accuracy to reconstruct the shape of the heated area. The averaged IE and DL are 2.39% and 3.16% respectively, which is acceptable considering the temporal resolution improvement compromises the loss of spatial resolution. On the contrary, the Kalman filter method cannot provide reasonable results due to its slow convergence nature. The reconstructed images have large reconstruction error and the dynamic features are poorly preserved.

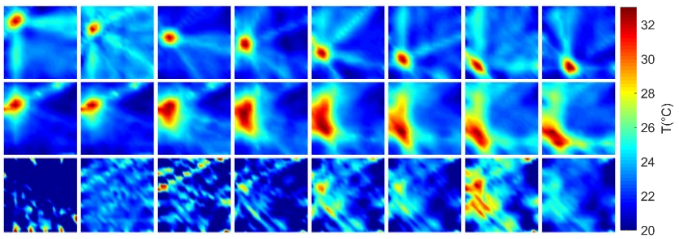

Figure 9: Fully sampled reconstruction results (top), the under-sampled reconstruction using OTRR (middle) and Kalman filter method (bottom)

Table 4: The averaged quantitative reconstruction metrics of the experiment results.

	IE (%)	PV (%)	DL (%)	WD
OTRR	2.39	0.96	3.16	3.54
Kalman	13.1	9.1	75	11.28

To validate the temperature reconstruction accuracy, a thermocouple was used to measure the temperature at the centre of the heated air steam. The results are showed in figure 10. The relative root mean square error (rRMSE) is 13.04% (with respect to Celsius) or 1.6% (with respect to Kelvin degree) at the centre of the reconstructed hotspot using 36 TOF measurements and the OTRR method. The Kalman filter method again has larger rRMSE 37.75% (with respect to Celsius) or 3.95% (with respect to Kelvin degree). On the other hand, the relative mean square error is much smaller using 192 TOFs and SIRT method, which is 6.58% (with respect to Celsius) or 0.66% (with respect to Kelvin degree).

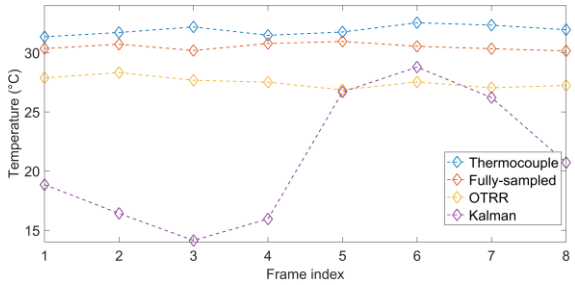

Figure 10: Comparison between the thermocouple measured temperature and tomographic reconstructed temperature.

V. Conclusion

In this paper, we developed an online time-resolved reconstruction (OTRR) method for real-time monitoring system. The proposed OTRR method can resolve the dynamic changes with a reduced number of TOFs. As a result, the measuring time per frame is reduced from 320 ms to 60 ms.

Based on the simulation results, OTRR has higher quantitative accuracy, faster convergence rate and better noise robustness compared to the Kalman based reconstruction method. From the experiments, the OTRR method provides satisfactory results in tracking the dynamic changes of the temperature field.

However, the proposed OTRR method also has the drawbacks of over-smoothing between successive frames. The improvement of the temporal resolution is at the cost of spatial resolution. It affects the quantitative accuracy of the temperature field reconstruction. Future work is to consider the dynamic temperature field evolution property and design the temporal regularization for specific applications.

VI. REFERENCE

[1] Y. Bao and J. Jia, "Improved time-of-flight estimation method for acoustic tomography system," *IEEE Transactions on Instrumentation and Measurement,* pp. 1-1, 2019.

[2] S. Liu, S. Liu, and T. Ren, "Acoustic Tomography Reconstruction Method for the Temperature Distribution Measurement," *IEEE Transactions on Instrumentation and Measurement,* 2017.

[3] P. Holstein, A. Raabe, R. Müller, M. Barth, D. Mackenzie, and E. Starke, "Acoustic tomography on the basis of travel-time measurement," *Measurement Science and Technology,* vol. 15, p. 1420, Jun 2004.

[4] I. Jovanovic, L. Sbaiz, and M. Vetterli, "Acoustic tomography for scalar and vector fields: theory and application to temperature and wind estimation," *Journal of Atmospheric and Oceanic Technology,* vol. 26, pp. 1475-1492, 2009.

[5] M. Barth and A. Raabe, "Acoustic tomographic imaging of temperature and flow fields in air," *Measurement Science and Technology,* vol. 22, p. 035102, Jan 2011.

[6] S. Zhang, G. Shen, L. An, and Y. Niu, "Online monitoring of the two-dimensional temperature field in a boiler furnace based on acoustic computed tomography," *Applied Thermal Engineering,* vol. 75, pp. 958-966, 2015.

[7] S. Zhang, G. Shen, L. An, and G. Li, "Ash fouling monitoring based on acoustic pyrometry in boiler furnaces," *Applied Thermal Engineering,* vol. 84, pp. 74-81, 2015.

[8] C. Li, N. Duric, P. Littrup, and L. Huang, "In vivo breast sound-speed imaging with ultrasound tomography," *Ultrasound in Medicine and Biology,* vol. 35, pp. 1615-1628, Oct 2009.

[9] A. Hormati, I. Jovanovic, O. Roy, and M. Vetterli, "Robust ultrasound travel-time tomography using the bent ray model," in *Proc. SPIE*, 2010, p. 76290I.

[10] I. Toši, I. Jovanovi, P. Frossard, M. Vetterli, and N. Duri, "Ultrasound tomography with learned dictionaries," in *2010 IEEE International Conference on Acoustics, Speech and Signal Processing*, 2010, pp. 5502-5505.

[11] R. van Sloun, A. Pandharipande, M. Mischi, and L. Demi, "Compressed sensing for ultrasound computed tomography," *IEEE Transactions on Biomedical Engineering,* vol. 62, pp. 1660-1664, 2015.

[12] N. Taniguchi, C.-F. Huang, A. Kaneko, C.-T. Liu, B. M. Howe, Y.-H. Wang*, et al.*, "Measuring the Kuroshio Current with ocean acoustic tomography," *The Journal of the Acoustical Society of America,* vol. 134, pp. 3272-3281, Oct 2013.

[13] S. G. Lingala, Y. Hu, E. DiBella, and M. Jacob, "Accelerated dynamic MRI exploiting sparsity and low-rank structure: kt SLR," *IEEE transactions on medical imaging,* vol. 30, pp. 1042-1054, May 2011.

[14] D. Kazantsev, G. Van Eyndhoven, W. Lionheart, P. Withers, K. Dobson, S. McDonald*, et al.*, "Employing temporal self-similarity across the entire time domain in computed tomography reconstruction," *Phil. Trans. R. Soc. A,* vol. 373, p. 20140389, Jun 2015.

[15] Y. Li, S. Liu, and S. H. Inaki, "Dynamic Reconstruction Algorithm of Three-Dimensional Temperature Field Measurement by Acoustic Tomography," *Sensors,* vol. 17, p. 2084, Jun 2017.

[16] B. Chen, J. F. Abascal, and M. Soleimani, "Electrical Resistance Tomography for Visualization of Moving Objects Using a Spatiotemporal Total Variation Regularization Algorithm," *Sensors,* vol. 18, p. 1704, May 2018.

[17] Z. Tian, X. Jia, B. Dong, Y. Lou, and S. B. Jiang, "Low‐dose 4DCT reconstruction via temporal nonlocal means," *Medical physics,* vol. 38, pp. 1359-1365, Mar 2011.

[18] K. A. Mohan, S. Venkatakrishnan, J. W. Gibbs, E. B. Gulsoy, X. Xiao, M. De Graef*, et al.*, "TIMBIR: A method for time-space reconstruction from interlaced views," *IEEE Trans. Computational Imaging,* vol. 1, pp. 96-111, 2015.

[19] A. Majumdar and R. K. Ward, "Causal dynamic MRI reconstruction via nuclear norm minimization," *Magnetic resonance imaging,* vol. 30, pp. 1483-1494, Dec 2012.

[20] Z.-P. Liang, "Spatiotemporal imaging with partially separable functions," in *Biomedical Imaging: From Nano to Macro, 2007. ISBI 2007. 4th IEEE International Symposium on*, 2007, pp. 988-991.

[21] H. Pedersen, S. Kozerke, S. Ringgaard, K. Nehrke, and W. Y. Kim, "k‐t PCA: temporally constrained k‐t BLAST reconstruction using principal component analysis," *Magnetic resonance in medicine,* vol. 62, pp. 706-716, 2009.

[22] D. Liang, E. V. DiBella, R. R. Chen, and L. Ying, "k‐t ISD: dynamic cardiac MR imaging using compressed sensing with iterative support detection," *Magnetic resonance in medicine,* vol. 68, pp. 41-53, 2012.

[23] S. Kolouri, M. R. Azimi-Sadjadi, and A. Ziemann, "Acoustic tomography of the atmosphere using unscented Kalman filter," *IEEE Transactions on Geoscience and Remote Sensing,* vol. 52, pp. 2159-2171, 2014.

[24] M. Soleimani, M. Vauhkonen, W. Yang, A. Peyton, B. S. Kim, and X. Ma, "Dynamic imaging in electrical capacitance tomography and electromagnetic induction tomography using a Kalman filter," *Measurement Science and Technology,* vol. 18, p. 3287, Sep 2007.

[25] A. Ziemann, K. Arnold, and A. Raabe, "Acoustic tomography as a method to identify small-scale land surface characteristics," *Acta Acustica united with Acustica,* vol. 87, pp. 731-737, 2001.

[26] Y. Bao, J. Jia, and N. Polydorides, "Real-time temperature field measurement based on acoustic tomography," *Measurement Science and Technology,* vol. 28, p. 074002, Jun 2017.

[27] P. L. Combettes and V. R. Wajs, "Signal recovery by proximal forward-backward splitting," *Multiscale Modeling & Simulation,* vol. 4, pp. 1168-1200, 2005.

[28] U. Sumbul, J. M. Santos, and J. M. Pauly, "A practical acceleration algorithm for real-time imaging," *IEEE transactions on medical imaging,* vol. 28, pp. 2042-2051, 2009.

[29] S. Kolouri, M. R. Azimi-Sadjadi, and A. Ziemann, "A statistical-based approach for acoustic tomography of the atmosphere," *The Journal of the Acoustical Society of America,* vol. 135, pp. 104-114, 2014.